difference in circumferences, the distance between sulfur and molybdenum atoms in the nanotube is virtually equal to the corresponding distance in plate-like crystals of MoS_2 (*21*). The dihedral S-Mo-S angle is 63° and 66° for the inner and outer layers, respectively. For comparison, in plate-like crystals, the dihedral angle is 81.5° (*22*). The close position of molybdenum and sulfur atoms in neighboring layers perpendicular to the nanotube axis requires an extension of the unit cell along the tube axis by at least 25% to avoid overlap of the covalent radii. Considering such an extension, the distance between the layers is 0.20 nm, corresponding to the diffraction data.

The unit cell of the hexagonal close-packed nanotubes within a bundle is 0.40 nm along the bundle axis and 0.96 nm perpendicular to the bundle axis. The closest sulfur atoms on adjacent nanotubes are separated by 0.35(1) nm, which corresponds approximately to their Van der Waals diameters. Iodine atoms are inserted in interstitial trigonal voids between the nanotubes, creating one-dimensional rows along the bundle axis. The periodicity of feasible sites for iodine position along the bundle is 0.40 nm, which is slightly less than the Van der Waals distance for iodine (0.43 nm).

High-resolution simulations (Fig. 2B, inset, and Fig. 3A, inset) using the symmetry operations of Group $P6_3$ (C_6^6)–No. 173 are found in agreement with the observed high-resolution images. The unit cell contains 6 molybdenum atoms and 12 sulfur atoms. The electron diffraction pattern (Fig. 3C) is indexed using calculated interlayer distances of the model structure. A comparison of the interlayer distances measured by x-ray and electron diffraction with the calculated values is presented in Table 1.

The presence of C_{60} in the growth process was found to be essential, and the nanotubes do not grow in its absence, but the detailed growth mechanism is not clear at present. We remark on the fact that the (1,1,1) plane of C_{60} crystals shows a hexagonal pattern with the in-plane lattice parameter of 1.004 nm (*23*), which is a close, but not perfect, match to the nanotube crystal lattice shown in Fig. 2A. It is quite conceivable that C_{60} plays an active role in promoting growth at the tip of the growing nanotube.

Table 1. Comparison of x-ray and TED diffraction results. Assignment for a hexagonal lattice: a = 0.96(1) nm, c = 0.4 nm.

Measured *d* (nm) ± 0.01 nm	Calculated *d* (nm)	Assignment (hkl)
0.83	0.831	100
0.35	0.36	101
0.31	0.307	111
0.28	0.277	300
0.2	0.2	002

Recently, large-diameter armchair MoS_2 nanotubes were predicted on the basis of density-functional tight-binding calculations (*24*) to be semiconducting with either a direct or an indirect bandgap, depending on their diameter and structure. Extrapolating these predictions to the (3,3) tubes discussed here, we can expect the indirect gap to close, giving rise to a metal with a small, but finite, density of states at E_F. However, the effect of confinement of electrons on the very narrow tubes is expected to give rise to energy level quantization for electrons hopping perpendicular to the tube axis which, because of the small diameters, may be expected to persist to unusually high temperatures.

Because of their efficient growth properties, the tubes may give rise to a new chalcogenide-nanotube technology based on their low-dimensional properties. The self-assembly into various regular geometrical shapes on different length scales appears to be a property unique to the MoS_2 SWNTs. The possibility of handling single tubes, such as was already demonstrated here, should facilitate investigation of single-tube properties, including quantum effects, in more detail.

References and Notes

1. M. Bockrath *et al.*, *Nature* **397**, 598 (1999).
2. A. Bachtold *et al.*, *Nature* **389**, 582 (1999).
3. W. A. de Heer, A. Châtelain, D. Ugarte, *Science* **270**, 1179 (1995).
4. M. M. J. Treacy, T. W. Ebbesen, J. M. Gibson, *Nature* **381**, 678 (1996).
5. R. Tenne *et al.*, *Nature* **360**, 444 (1992).
6. L. Margulis *et al.*, *Nature* **365**, 113 (1993).
7. R. Tenne *et al.*, *Chem. Mater.* **10**, 3225 (1999).
8. A. Zak, Y. Feldman, V. Alperovich, R. Rosentsveig, R. Tenne, *J. Am. Chem. Soc.* **122**, 11108 (2000).
9. M. Remskar, Z. Skraba, F. Cleton, R. Sanjines, F. Levy, *Appl. Phys. Lett.* **69**, 351 (1996).
10. M. Remskar *et al.*, *Adv. Mater.* **10**, 246 (1998).
11. M. Remskar, Z. Skraba, R. Sanjines, F. Levy, *Appl. Phys. Lett.* **74**, 633 (1999).
12. Y. Golan *et al.*, *Adv. Mater.* **11**, 934 (1999).
13. M. Chhowalla, G. A. J. Amaratunga, *Nature* **407**, 164 (2000).
14. N. G. Chopra *et al.*, *Science* **269**, 966 (1995).
15. M. Terrones *et al.*, *Chem. Phys. Lett.* **259**, 568 (1996).
16. W. B. Hu *et al.*, *Appl. Phys. A* **70**, 231 (2000).
17. Y. Rosenfeld Hacohen, E. Grunbaum, R. Tenne, J. Sloan, J. L. Hutchison, *Nature* **395**, 336 (1998).
18. G. Seifert, H. Terrones, M. Terrones, T. Frauenheim, *Solid State Commun.* **115**, 635 (2000).
19. M. Côté, M. L. Cohen, D. J. Chadi, *Phys. Rev. B* **58**, R4277 (1998).
20. The structure of the transported material was studied using 300-keV Philips CM300, Jeol JEM-2010F, and Philips XL 30FEG electron microscopes and Hitachi HF-2000 equipped with EELS. X-ray structural analysis has been used for confirmation of electron diffraction data and x-ray fluorescence spectrometry for composition analysis.
21. M. S. Dresselhaus, G. Dresselhaus, P. C. Ecklund, *Science of Fullerenes and Carbon Nanotubes* (Academic Press, New York, 1996).
22. J. A. Wilson, A. D. Yoffe, *Adv. Phys.* **18**, 193 (1969).
23. W. Krätschmer, L. D. Lamb, K. Fostiropoulos, D. R. Huffman, *Nature* **347**, 354 (1990).
24. G. Siefert, H. Terrones, M. Terrones, G. Jungnickel, T. Frauenheim, *Phys. Rev. Lett.* **85**, 146 (2000).

25. We thank M. Cantoni and G. Drazic for help in electron microscopy and P. Kump for x-ray fluorescence measurements. We are also sincerely grateful G. Seifert and H. Cohen for useful discussions.

12 January 2001; accepted 9 March 2001

Probing the Structure of Metal Cluster–Adsorbate Systems with High-Resolution Infrared Spectroscopy

K. Nauta, D. T. Moore, P. L. Stiles, R. E. Miller*

High-resolution infrared laser spectroscopy was used to obtain rotationally resolved infrared spectra of adsorbate-metal complexes. The method involves forming the bare metal clusters in helium nanodroplets and then adding a molecular adsorbate (HCN) and recording the infrared spectrum associated with the C-H stretching vibration. Rotationally resolved spectra were obtained for HCN-Mg_n (n = 1 to 4). The results suggest a qualitative change in the adsorbate–metal cluster bonding with cluster size.

The vibrational dynamics of molecules adsorbed on metal surfaces is of fundamental interest (*1*) and great practical importance to several fields, for example, catalysis (*2*, *3*). Infrared (IR) spectroscopy has been widely used to study such processes (*1*), with the goal of understanding the associated molecule-surface interactions. Although studies of this type have provided important insights into the nature of the associated interactions, progress has been hampered because the theoretical methods used to interpret the experimental data have trouble dealing with the large number of surface atoms (*4*). In most cases, this problem has been addressed by

---

Department of Chemistry, University of North Carolina, Chapel Hill, NC 27599, USA.

*To whom correspondence should be addressed. E-mail: remiller@unc.edu

approximating the surface with a cluster of metal atoms embedded in a semi-infinite solid (*4*). Ideally, ab initio calculations would be tested against experimental vibrational frequencies of adsorbate molecules on free metal clusters of known sizes and structures. Unfortunately, rotationally resolved vibrational spectra, which can provide detailed information concerning structure and bonding, have not previously been available for these systems. Data of this type would be particularly valuable given that the reactivity of metal clusters has been shown to be highly dependent on size, as illustrated by studies of magnesium clusters with methyl halides (*5*). However, these experiments did not provide direct structural information on these systems. We report here a general method for obtaining high-resolution (rotationally resolved) IR spectra of metal-adsorbate complexes, from which structures can be determined.

The metal clusters of interest were formed in helium nanodroplets. Superfluid helium droplet spectroscopy (SHEDS) was demonstrated by the group of Scoles (*6*) and has undergone rapid development in a number of laboratories (*7–9*). It is now well established that the droplets cool by evaporation to a temperature of 0.37 K. Atoms and molecules are easily introduced into the helium by passing the droplets through a pick-up cell (*10*), maintained at a sufficiently high pressure to ensure that these gas-phase dopants collide with and are captured by the droplets. The solvation environment inside the droplets is quite homogeneous and weakly interacting, which makes it ideal for spectroscopy (*11*). The superfluid nature of the droplets slows the relaxation processes that would otherwise broaden the corresponding spectra and prevent the observation of rotational fine structure.

Neutral (neat) magnesium clusters have been the subject of considerable experimental (*5*, *12*, *13*) and theoretical (*14–16*) study. They were chosen here as a first case for study because of the relative ease with which magnesium can be volatilized and because it has no unpaired electrons, which makes the spectroscopy more straightforward. Although pure metal clusters have previously been grown in helium droplets (*17*, *18*), IR spectra of adsorbed species on metal clusters have not been reported.

The apparatus used in the present study has been discussed in some detail elsewhere (*19*). The droplets capture one or more magnesium atoms in a small metal oven at about 300°C (corresponding to an Mg vapor pressure of 10^{-5} torr). HCN is subsequently added by passing the droplets through a second pick-up chamber, so that the complexes of interest are formed. Given the fast cooling provided by the liquid helium, the metal clusters formed in the first pick-up region are cold before the HCN is added. In previous studies of cluster growth in liquid helium droplets, we have shown that the resulting structures are consistent with this type of sequential addition of cold species (*8*, *20*). The IR spectra of the HCN-magnesium clusters, corresponding to the excitation of the C-H stretch, were recorded with an F-center laser (*21*). Vibrational relaxation of the complexes by the liquid helium resulted in the evaporation of about 600 helium atoms, and the associated depletion of the droplet beam was measured with a bolometer detector (*21*). Two electrodes were positioned so that a large dc electric field could be applied to the laser excitation region. As shown previously (*22*, *23*), the applied field collapses the entire ro-vibrational band of a polar molecule into a single, intense peak (a pendular spectrum), which aids in the detection and identification of species.

At the low temperatures of the helium droplets, we expect that the magnesium will form weakly bound complexes with the HCN and leave the C-H stretch relatively unperturbed, thus making the corresponding spectral search straightforward. The first spectra were recorded with an applied dc electric field and the oven at room temperature. Under these conditions, neat HCN clusters were grown in the droplets (*8*), as shown in Fig. 1A. This region of the spectrum, corresponding to the free C-H stretch, was then repeatedly scanned as the temperature of the metal oven was increased. No substantial changes in the spectrum were observed until the oven temperature was sufficiently high to evaporate magnesium, at which point the spectrum changed to that shown in Fig. 1B. We assigned these features to complexes containing a single HCN molecule, bound to Mg clusters of different sizes. These assignments are justified on the basis of the following considerations: (i) The dependence of the signals on the HCN partial pressure confirms that these complexes all contain a single HCN molecule, (ii) the strong field dependence of these peaks confirms that the associated complexes are polar, and (iii) at higher oven temperatures, the peaks assigned to larger magnesium clusters increase in intensity at the expense of the smaller ones. The bands associated with clusters containing multiple HCN molecules are very weak in Fig. 1B because the conditions were reoptimized for the pick-up of a single HCN molecule.

The next step in the assignment of the above spectra involved turning off the dc electric field, so that the rotational fine structure could be observed in each of the bands. The signals are considerably weaker in this case but still sufficient to obtain the spectra shown in Fig. 2 for the band assigned to HCN-Mg. This spectrum shows only P- and R-branches, consistent with a linear (vibrationally averaged) complex, as shown in the inset. This spectrum was fit to a linear molecule energy level expression, yielding the calculated spectrum in Fig. 2. The resulting ground vibrational state rotational constant is 0.0285 cm^{-1}, and the vibrational origin is 3309.35 cm^{-1}. This spectrum was obtained with the use of relatively large droplets (~8000 atoms) in an effort to reduce the effects of inhomogeneous broadening (*24*). For smaller droplets, where the inhomogeneities are greater (*20*, *25*), we observed that the transitions near the vibrational origin were poorly resolved.

The redshift of this band from the HCN vibrational origin in helium (*26*) is only 1.89 cm^{-1}. This small shift is consistent with a "free" CH stretch, indicating that the Mg atom binds to the N-end of the HCN (*8*). This structure is consistent with an ab initio potential [CCSD(T)/6-311++G(3df,3pd)] we have generated for HCN-Mg (*27*), which shows that the Mg binds more strongly at the N-end (−147 cm^{-1}) than at the H-end (−124 cm^{-1}). The calculated Mg to HCN center-of-mass distances are 4.5 and 5.4 Å, for the N- and H-end minima, respectively. Comparison of the ab initio and experimental rotational constants is complicated by the contribution made by the helium to the moment of inertia of the complex (*28–30*), and a quantitative correction for this effect will require a considerable theoretical effort. However, we have compiled a large database of rotational constants for molecules and complexes in helium (*31*), and our experience indicates that, when the gas-phase rotational constant is smaller than about 0.25 cm^{-1}, the ratio of the gas-phase and helium droplet constants is 2.5 ± 0.5. The corresponding ratios based on the ab initio calculations for the magnesium

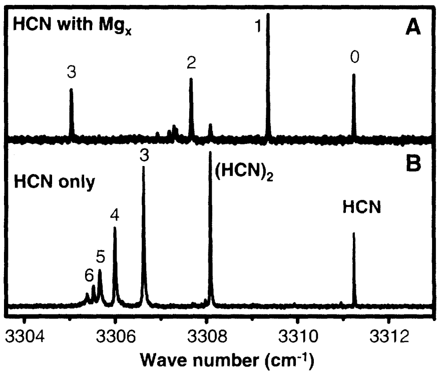

Fig. 1. (**A**) A pendular state spectrum of the free C-H stretch of linear HCN clusters [the labels corresponding to (HCN)$_n$] grown in liquid helium, with the magnesium oven at room temperature. (**B**) A pendular state spectrum obtained with the magnesium oven at high temperature. All of the numbered peaks correspond to complexes containing a single HCN molecule and the indicated number of magnesium atoms.

bound to the N-end and H-end of HCN are ~2.3 and ~1.5, respectively, providing further evidence for the HCN-Mg structure. An interesting side note is that matrix-isolation studies of the reaction of Mg atoms with HCN reveal only the CNMg product and not MgCN (*32*).

A zero field spectrum of the band we have assigned here to HCN-Mg_2 was also recorded. This spectrum (*27*) has a strong Q-branch, consistent with the T-shaped structure we obtained from ab initio calculations. This is a fairly asymmetric rotor and the corresponding spectrum is only partially resolved. Nevertheless, our preliminary estimates of the rotational constants for this complex are in good agreement with the results of ab initio calculations, when the correction factor corresponding to solvation in helium is applied, and the adsorbate–metal cluster distance is comparable to the calculated value for HCN-Mg.

Figure 3 shows a rotationally resolved (zero field) spectrum corresponding to the HCN-Mg_3 pendular peak. This spectrum is consistent with a parallel band of a symmetric top, suggesting that the Mg_3 atoms are in a trigonal planar geometry, with the HCN along the threefold axis, as shown in the figure inset. The calculated spectrum in Fig. 3 was generated with a prolate symmetric top Hamiltonian with $A = 0.035\ \mathrm{cm}^{-1}$ and $B = 0.0167\ \mathrm{cm}^{-1}$, taking into account the C_{3v} spin statistics associated with such a structure. This assignment was checked with ab initio calculations (*33*), which gave a minimum (about $-1050\ \mathrm{cm}^{-1}$) with the HCN center of mass ~3.6 Å above the Mg_3 plane (see Fig. 3 inset). The calculated rotational constants for this minimum are $A = 0.064\ \mathrm{cm}^{-1}$ and $B = 0.0431\ \mathrm{cm}^{-1}$, corresponding to a gas-phase/helium ratio of 2.6 for the B constants, which is again reasonable given the above discussion.

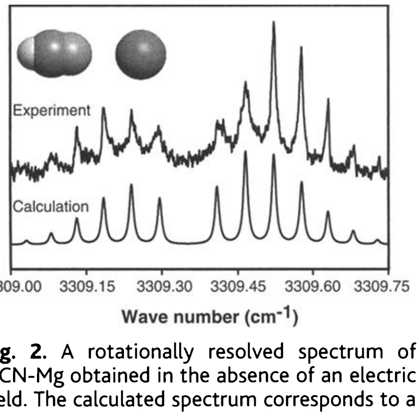

Fig. 2. A rotationally resolved spectrum of HCN-Mg obtained in the absence of an electric field. The calculated spectrum corresponds to a fit to a linear molecule energy level expression, the intensities corresponding to a rotational temperature of 0.37 K. The rotational constant obtained from the fit is $0.0285\ \mathrm{cm}^{-1}$ for the vibrational ground state, and the vibrational origin is $3309.35\ \mathrm{cm}^{-1}$.

The theoretical studies on pure magnesium clusters have shown that many-body effects are extremely important. For example, calculations indicate that the Mg-Mg bond distance shrinks by 0.6 Å in going from Mg_2 to Mg_3 (*16*). The effects of these changes are evident in our data on the HCN-Mg_n clusters. First, it is striking that the difference in redshift between the Mg_2 and Mg_3 complexes is greater than the difference in redshift between Mg_1 and Mg_2 (Fig. 1B). This result is contrary to our size-dependent studies of rare gas clusters with HCN and HF, where the sequential vibrational frequency shifts converge smoothly to limiting values (*34*). The spectra of the HCN chains also show a smooth dependence on cluster size, the "free" C-H stretch being less and less affected by the addition of subsequent molecules in the chain. We have preliminary data on HCN-Mg_4 that show an even more marked shift, emphasizing the nonadditivity of the interactions.

Further evidence for this nonadditivity comes from comparing the rotational constants of the three complexes and correlating them to structural differences seen in the calculations. Our best estimates for the rotational constant of the HCN-Mg_2 complex indicate that, although it is substantially smaller than that for HCN-Mg, is it only slightly larger than that for the HCN-Mg_3. The reason for this can be seen in the calculated N-Mg distances for the complexes (*35*); in HCN-Mg and HCN-Mg_2, this distance is ~3.8 Å, whereas in HCN-Mg_3, it contracts to 3.5 Å, a difference of 0.3 Å. This large change again emphasizes the fact that the interactions in these systems are strongly nonadditive and that the two-body interactions cannot be assumed to dominate. This is in agreement with the results of Higgins *et al.* (*17*) on spin-polarized alkali clusters, which indicate that 80% of the trimer binding comes from nonadditive effects.

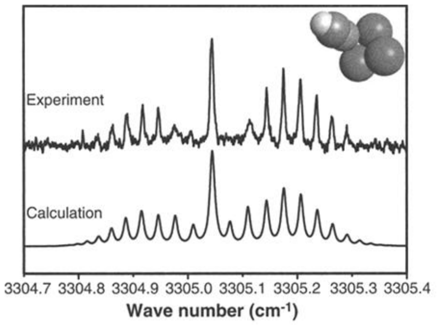

Fig. 3. A rotationally resolved spectrum of the HCN-Mg_3 complex. The calculated spectrum includes the nuclear spin statistics corresponding to the C_{3v} symmetry of the complex. The simulated spectrum is based on a symmetric top calculation with $A = 0.035\ \mathrm{cm}^{-1}$ and $B = 0.0167\ \mathrm{cm}^{-1}$ as rotational constants for the vibrational ground state, and the vibrational origin is $3305.04\ \mathrm{cm}^{-1}$. The A rotational constant was adjusted to fit the intensity of the Q-branch relative to the P- and R-branches.

At this point, it is certainly premature to suggest that this strong nonadditivity is the result of chemical interactions or indicative of the onset of metallic behavior. In fact, recent work on bare magnesium clusters by Thomas *et al.* (*36*), using negative ion photoelectron spectroscopy, shows that metallic behavior (closing of the HOMO-LUMO gap) is not observed until the size range $Mg_{18\text{-}19}$ is reached. This would suggest that the effects we observed here are not directly related to the onset of metallic properties. Indeed, calculations by Scoles *et al.* (*37*) on pure magnesium clusters indicate that nonadditive repulsion plays a crucial role. A detailed understanding of these effects will clearly require further theoretical studies aimed at isolating the various contributions to the overall interaction potential.

The present results on the vibrational spectroscopy of molecules bound to metal clusters show that the nonadditive effects characteristic of bare metal clusters are also reflected in their interaction with adsorbates and that the systematic study of the adsorbate vibrational frequencies as a function of metal cluster size is a powerful approach for studying these effects.

References and Notes

1. Y. T. Chabal, *Surf. Sci. Rep.* **8**, 211 (1988).
2. M. Moskovits, *Acc. Chem. Res.* **12**, 229 (1979).
3. K. J. Klabunde, *Free Atoms, Clusters and Nanoscale Particles* (Academic Press, New York, 1994).
4. J. L. Whitten, H. Yang, *Surf. Sci. Rep.* **218**, 55 (1996).
5. Y. Imizu, K. J. Klabunde, *Inorg. Chem.* **23**, 3602 (1984).
6. S. Goyal, D. L. Schutt, G. Scoles, *Phys. Rev. Lett.* **69**, 933 (1992).
7. M. Hartmann, R. E. Miller, J. P. Toennies, A. F. Vilesov, *Science* **272**, 1631 (1996).
8. K. Nauta, R. E. Miller, *Science* **283**, 1895 (1999).
9. C. Kim, S. Yurgenson, J. A. Northby, *Z. Phys. D Atoms Mol. Clusters* **40**, 119 (1997).
10. T. E. Gough, M. Mengel, P. Rowntree, G. Scoles, *Proc. SPIE Int. Soc. Opt. Eng.* **669**, 129 (1986).
11. K. K. Lehmann, G. Scoles, *Science* **279**, 2065 (1998).
12. M. Elhanine *et al.*, *J. Chem. Phys.* **112**, 10912 (2000).
13. C. Crepin-Glibert, A. Tramer, *Int. Rev. Phys. Chem.* **18**, 485 (1999).
14. P. Ballore, W. Andreoni, in *Metal Clusters*, W. Ekardt, Ed. (Wiley, West Sussex, UK, 1999), pp. 71–136.
15. C. W. Bauschlicher, H. Partridge, *Chem. Phys. Lett.* **300**, 364 (1999).
16. I. G. Kaplan, S. Roszak, J. Leszczynski, *J. Chem. Phys.* **113**, 6245 (2000).
17. J. Higgins *et al.*, *Phys. Rev. Lett.* **77**, 4532 (1996).
18. J. Higgins *et al.*, *J. Phys. Chem. A* **102**, 4952 (1998).
19. K. Nauta, R. E. Miller, *J. Chem. Phys.* **111**, 3426 (1999). Helium droplets are formed in an expansion of high-pressure (~60 bar) ultrapure helium through a 5-μm-diameter nozzle cooled to about 22 K, producing droplets with an average size of 3000 atoms. To produce larger droplets, we lowered the nozzle temperature to about 18.5 K.
20. K. Nauta, D. T. Moore, R. E. Miller, *Faraday Discuss. Chem. Soc.* **113**, 261 (1999).
21. Z. S. Huang, K. W. Jucks, R. E. Miller, *J. Chem. Phys.* **85**, 3338 (1986).
22. P. A. Block, E. J. Bohac, R. E. Miller, *Phys. Rev. Lett.* **68**, 1303 (1992).
23. J. M. Rost, J. C. Griffin, B. Friedrich, D. R. Herschbach, *Phys. Rev. Lett.* **68**, 1299 (1992).
24. C. Callegari *et al.*, *J. Chem. Phys.* **113**, 4636 (2000).

25. S. Grebenev *et al.*, *J. Chem. Phys.* **112**, 4485 (2000).
26. K. Nauta, R. E. Miller, *Phys. Rev. Lett.* **82**, 4480 (1999).
27. P. L. Stiles, D. T. Moore, K. Nauta, R. E. Miller, in preparation.
28. M. Hartmann, R. E. Miller, J. P. Toennies, A. F. Vilesov, *Phys. Rev. Lett.* **75**, 1566 (1995).
29. C. Callegari *et al.*, *Phys. Rev. Lett.* **83**, 5058 (1999).
30. Y. Kwon, P. Huang, M. V. Patel, D. Blume, K. B. Whaley, *J. Chem. Phys.* **113**, 6469 (2000).
31. K. Nauta, thesis, University of North Carolina at Chapel Hill (2000).
32. D. V. Lanzisera, L. Andrews, *J. Phys. Chem. A* **101**, 9666 (1997).
33. Points on the potential energy surface were calculated [MP2/6-311++G(2df,2pd)] with the Mg atoms fixed in the equilibrium trimer geometry (*24*). The distance of the HCN from the Mg$_3$ plane was varied, as was the angle made by the HCN with the Mg$_3$ plane.
34. K. Nauta, R. E. Miller, in preparation.
35. The N-Mg distances for HCN-Mg and HCN-Mg$_2$ are taken from MP2/6-311++G(3df,3pd) geometry optimizations, whereas the distance for HCN-Mg$_3$ is interpolated from the PES scan described in (*34*).
36. O. C. Thomas, W. Zheng, K. H. Bowen, private communication.
37. J. M. Sin, S. Nayak, G. Scoles, in *Cluster and Nanostructure Interfaces*, P. Jena, S. N. Khanna, B. K. Rao, Eds. (World Scientific, Singapore, 2000), pp. 345–352.
38. This work was supported by the NSF (CHE-99-87740). We also acknowledge the donors of the Petroleum Research Fund, administered by the American Chemical Society, and the Air Force Office for Scientific Research (AFOSR) for partial support of this research. We thank G. Scoles for helpful discussions during the preparation of this manuscript and K. H. Bowen for permitting us to quote his results as a private communication.

11 January 2001; accepted 6 March 2001

Imaging of Small-Scale Features on 433 Eros from NEAR: Evidence for a Complex Regolith

J. Veverka,[1] P. C. Thomas,[1] M. Robinson,[2] S. Murchie,[3] C. Chapman,[4] M. Bell,[1] A. Harch,[1] W. J. Merline,[4] J. F. Bell III,[1] B. Bussey,[2] B. Carcich,[1] A. Cheng,[3] B. Clark,[1] D. Domingue,[3] D. Dunham,[3] R. Farquhar,[3] M. J. Gaffey,[5] E. Hawkins,[3] N. Izenberg,[3] J. Joseph,[1] R. Kirk,[6] H. Li,[2] P. Lucey,[7] M. Malin,[8] L. McFadden,[9] J. K. Miller,[10] W. M. Owen Jr.,[10] C. Peterson,[1] L. Prockter,[3] J. Warren,[3] D. Wellnitz,[9] B. G. Williams,[10] D. K. Yeomans[10]

On 25 October 2000, the Near Earth Asteroid Rendevous (NEAR)–Shoemaker spacecraft executed a low-altitude flyover of asteroid 433 Eros, making it possible to image the surface at a resolution of about 1 meter per pixel. The images reveal an evolved surface distinguished by an abundance of ejecta blocks, a dearth of small craters, and smooth material infilling some topographic lows. The subdued appearance of craters of different diameters and the variety of blocks and different degrees of their burial suggest that ejecta from several impact events blanketed the region imaged at closest approach and led to the building up of a substantial and complex regolith consisting of fine materials and abundant meter-sized blocks.

Data obtained during the early phases of NEAR's orbital mission answered many first-order questions about the global and regional characteristics of asteroid 433 Eros (*1*). These data confirmed that the surface is covered with regolith (*2*) and contained hints that the regolith is complex. To better understand the processes that have shaped the surface of Eros and determined the characteristics of its regolith, higher resolution images were needed.

On 25 October 2000, the NEAR spacecraft executed a low-altitude flyover (LAF), during which it swept down to 6.4 km above the surface of Eros, permitting the multispectral imager (MSI) camera to view the surface at a resolution of 1 m per pixel, which is about four times better than the best previous views. About 250 images were obtained during the LAF through the camera's 950-nm filter, in addition to two isolated three-color spot views using the 550-, 760-, and 950-nm filters (*3*). A narrow belt of coverage was obtained around Eros at mid-southern latitudes at altitudes below 30 km (resolution $\leq$4 m). Images obtained at altitudes below 10 km covered a thin strip between 34°S, 359°W to 4°S, 45°W. Closest approach (19.9°S, 27.8°W) occurred at an altitude of 6.43 km (with a resolution of about 1 m per pixel). The solar phase angle at closest approach was 97° (*4*). The only comparable data for airless bodies are images of the moon and the Mars satellite Phobos (*5*).

Our images reveal a complex surface marked by diverse evidence of regolith, a dearth of small impact craters, and an abundance of positive relief features (PRFs), most likely ejecta blocks (Fig. 1). The high-resolution images cover cratered terrains on Eros and do not cross into the two major depressions on the asteroid: the 9.4-km saddle Himeros and the 5.2-km crater Psyche (*1*). The images show a subdued, gently undulating surface characterized by abundant blocks and conspicuously degraded craters. Many of the degraded craters show evidence of infilling. A novel feature is the occurrence of smooth flat areas (hereafter referred to as ponds) in the interiors of certain craters (Fig. 2), features that to our knowledge have not been noted before in images of Phobos or of Deimos (*5*). No other asteroid has been imaged at comparable resolution. The region of high-resolution coverage is crossed in a few places by linear depressions ("grooves"), which can be traced out in previous lower resolution images.

Color observations obtained during the LAF show no difference between the colors of blocks and those of the surrounding regolith. Lower resolution images had shown albedo and color differences associated with steep slopes in certain regions, especially within the crater Psyche and the saddle Himeros (*6*). Two sets of three-color images at 550, 760, and 950 nm were acquired during the low-altitude flyover (*7*). One of the areas contains a large number of boulders and several smooth pond deposits. Most boulders in the size range of 5 to 10 m show no color difference from the background regolith, a finding consistent with results for larger boulders ($\sim$50 m) from earlier data obtained during the 50-km orbit (*6*). The ponds, on average, have a slightly higher 560/760-nm ratio (0.69 versus 0.67) and a slightly lower 950/760-nm ratio (0.94 versus 0.95), but the difference is very small and may not be signif-

---

[1] Space Sciences Building, Cornell University, Ithaca, NY 14853, USA. [2] Department of Geological Sciences, Northwestern University, 309 Locy Hall, Evanston, IL 60208, USA. [3] Applied Physics Laboratory, Johns Hopkins University, 1110 Johns Hopkins Road, Laurel, MD 20723, USA. [4] Southwest Research Institute, 1050 Walnut Street, Suite 426, Boulder, CO 80302, USA. [5] Department of Earth and Environmental Sciences, Science Center, Rensselaer Polytechnic Institute, 110 8th Street, Troy, NY 12180–3590, USA. [6] U.S. Geological Survey, 2255 North Gemini Drive, Flagstaff, AZ 86001, USA. [7] Hawaii Institute of Geophysics and Planetology, University of Hawaii, 2525 Correa Road, Honolulu, HI 96822, USA. [8] Malin Space Science Systems, Post Office Box 910148, San Diego, CA 92191, USA. [9] Department of Astronomy, University of Maryland, College Park, MD 20742, USA. [10] Jet Propulsion Laboratory, 4800 Oak Grove Drive, Pasadena, CA 91109, USA.